DEM Simulation of Uniaxial Compressive and Flexural Strength of Sea Ice: Parametric Study

Shunying Ji, Aff.M.ASCE[1]; Shaocheng Di[2]; and Xue Long[3]

Abstract: Microscale parameters have significant influence on the macromechanical behaviors of brittle materials in the discrete-element method (DEM). The rational determination of microparameters is still an open problem to model the failure characteristics of brittle materials. In this study, a three-dimensional DEM with bonded-particles is adopted to simulate the failure process of brittle materials. Interparticle friction and softening failure criteria are applied in the DEM simulations. The physical experimental data of sea ice are adopted to calibrate the DEM results. The influences of the interparticle friction coefficient and the bonding strength of bonded particles on the failure processes of sea ice are analyzed with the DEM simulations of the uniaxial compressive and flexural strengths of sea ice. The ratio of uniaxial compressive to flexural strength is used to calibrate the interparticle strengths and friction coefficient of bonded particles in comparison with experimental data. The relationship between interparticle strength and macrostrength are determined based on the DEM results. **DOI: 10.1061/(ASCE)EM.1943-7889.0000996.** *© 2016 American Society of Civil Engineers.*

Author keywords: Discrete-element method (DEM); Bonded particles; Uniaxial compressive strength; Flexural strength; Brittle material; Sea ice.

Introduction

Nowadays, the discrete-element method (DEM) with bonded particles has been applied to simulate the failure process of brittle materials, such as rock, concrete, and sea ice (Potyondy and Cundall 2004; Scholtes and Donze 2012; Weerasekara et al. 2013; Estay and Chiang 2013; Lisjak and Grasselli 2014). In these DEM simulations, the continuum materials are constructed with two dimensional (2D) disks or three dimensional (3D) spheres on the microscale. The computational parameters of bonded particles on the microscale, such as particle diameter, normal and shear stiffness, and tensile and shear bonding strength, are defined firstly in order to calculate the contact force and failure of bonded particles. The microscale computational parameters have significant influences on the simulated mechanical properties of brittle materials on the macro scale. In the last decade, the relationship between the microparameters and the simulated macrobehaviors has been investigated to determine the reliable input parameters in DEM simulations (Potyondy and Cundall 2004; Rojek et al. 2011; Lisjak and Grasselli 2014; Yan et al. 2015; Nitka and Tejchman 2015). Recently, physical experiments, such as uniaxial compressive, flexural, triaxial, and Brazilian tests, have been performed to calibrate the microparameters of brittle materials (Cho et al. 2007; Hanley et al. 2011).

The failure behaviors of brittle materials simulated with DEM are sensitively dependent on the particle size (Potyondy and Cundall 2004; Kuhn and Bagi 2009; Liu et al. 2012, 2013; Ding et al. 2014; Tarokh and Fakhimi 2014). With the sensitive analysis of size effect, the reasonable ratio of the sample size L to the particle diameter d can be determined. In DEM simulations, the contact force law and the boundary condition are quite different for various values of L/d. Thus, the DEM results are sensitively depended on L/d (Yang et al. 2006). Normally, the simulated Young's modulus and macrostrength increase with increasing L/d until $L/d > 30$, and then stay about the same (Ding et al. 2014). Recently, the coarse graining method is being introduced into DEM simulations to obtain high computational efficiency with good numerical precision (Feng and Owen 2014).

In the contact force model between bonded particles, the normal stiffness K_n can be defined simply with the diameter and elastic modulus of particles (Potyondy and Cundall 2004; Ergenzinger et al. 2012; Wang and Tonon 2010). Normally, the shear stiffness K_s is determined normally with the ratio of K_n/K_s. Potyondy and Cundall (2004) firstly set it as 2.5 to model the breakage of rock. This ratio is still used in the DEM simulation of breakage of rock materials (Cho et al. 2007; Ali and Bradshaw 2010; van Wyk et al. 2014). Recently, some researchers set this ratio to 1.0 (Hanley et al. 2011; Metzger and Glasser 2012; Hashemi et al. 2014; Yang et al. 2014), 2.0 (Yang et al. 2006; Park and Song 2009, 2013; Huang et al. 2014), 3.0 (Scholtes and Donze 2012; Ding et al. 2014), or 4.0 (Tarokh and Fakhimi 2014). This ratio of normal to shear stiffness affects both the Poisson's ratio and the failure strength of continuum materials on the macroscale (Yang et al. 2006; Tavarez and Plesha 2007). To obtain a reasonable Poisson's ratio of brittle materials, the value of this ratio can be more than 5.0, or even 100.0 (Wang and Tonon 2009, 2010; Rojek et al. 2011; Azevedo et al. 2015).

The bonding strength between particles on the microscale is another key parameter influencing the failure characteristics of brittle materials. The relationship between interparticle strength and macrostrength of continuum materials has been examined with DEM simulations. In the initial DEM investigation of bonded particles for rock breakage, the ratio of interparticle tensile strength σ_b^n to shear strength σ_b^s is set as 1.0 (Potyondy and Cundall 2004). This value has been widely used in the DEM simulations of failure process of

[1]Professor, State Key Laboratory of Structural Analysis for Industrial Equipment, Dalian Univ. of Technology, Dalian 116023, China (corresponding author). E-mail: jisy@dlut.edu.cn

[2]Doctoral Student, Dept. of Engineering Mechanics, Dalian Univ. of Technology, Dalian 116023, China.

[3]Doctoral Student, Dept. of Engineering Mechanics, Dalian Univ. of Technology, Dalian 116023, China.

Note. This manuscript was submitted on April 19, 2015; approved on July 17, 2015; published online on March 18, 2016. Discussion period open until August 18, 2016; separate discussions must be submitted for individual papers. This paper is part of the ***Journal of Engineering Mechanics***, © ASCE, ISSN 0733-9399.

continuum materials (Cho et al. 2007; Park and Song 2009, 2013; Ali and Bradshaw 2010; Hanley et al. 2011; Rojek et al. 2011; Metzger and Glasser 2012; Hashemi et al. 2014; van Wyk et al. 2014; Ding et al. 2014; Brown et al. 2014). However, different values are also used in some simulations (Yang et al. 2006, 2014; Tarokh and Fakhimi 2014). Moreover, some researchers adopt the tensile and compressive strengths to model the breakage of bonded particles, and the compressive strength is normally set 10 times larger than the tensile strength (Hosseininia and Mirghasemi 2007; Scholtes and Donze 2012; Ergenzinger et al. 2012). In previous studies, the interparticle shear bonding strength is independent of the normal contact force in DEM simulations. Recently, the influence of normal pressure on shear strength was considered and introduced into the failure criteria of bonded particles based on the Mohr-Coulomb friction law (Cho et al. 2007; Wang and Tonon 2010; Scholtes and Donze 2012; Estay and Chiang 2013; Nitka and Tejchman 2015). The rolling friction was also considered to improve the failure criteria of bonded particles in some DEM simulations (Wang 2009). Moreover, a tensile softening contact bond model is also developed to model the progressive failure process of brittle materials (Hentz et al. 2004; Wang and Tonon 2010; Tarokh and Fakhimi 2014; Azevedo et al. 2015).

In this study, the DEM with bonded particles are adopted to simulate the failure process of sea ice material, which behaves as a typical brittle material under a rapid loading rate. The failure criterion of bonded particles is developed with the consideration of the interparticle friction effect in order to obtain its reasonable uniaxial compressive strength and flexural strength. This paper focuses on the influence of interparticle bonding strength of failure processes of sea ice without changing the ratios of L/d and K_n/K_s. The ratio of interparticle tensile to shear strength and interparticle friction coefficient are determined by the comparison of the DEM results with the physical experimental data of sea ice.

Failure Criteria of Bonded Particles in DEM

To simulate the mechanical properties of continuum on the macroscale, the spherical particles are glued together with parallel bond model, as shown in Fig. 1. The parallel bond can be envisioned as a set of elastic springs with constant normal and shear stiffness, uniformly distributed over a circular disk lying on the contact plane and centered at the contact point (Potyondy and Cundall 2004). A parallel bond is defined by the following five parameters: normal and shear stiffness, K_n and K_s; interparticle normal and shear strength, σ_n^b and σ_s^b; and the bonding disk radius, R. Normally, R is set as the smaller radius of the two bonded particles(Potyondy and Cundall 2004) or their mean radius (Wang and Tonon 2009, 2010; Nitka and Jejchman 2015). The forces and moments in the normal direction and the shear direction associated with the parallel bond are denoted by F_n, F_s, M_n, and M_s. The maximum tensile and shear stresses acting on the bonding disk are calculated based on the beam theory as (Potyondy and Cundall 2004)

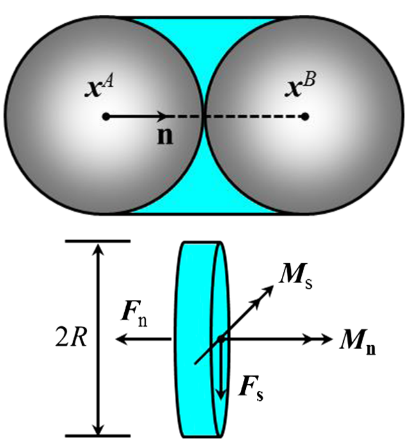

Fig. 1. Bonding model between two spherical particles

$$\sigma_{\max} = \frac{-F_n}{A} + \frac{|M_s|}{I}R, \qquad \tau_{\max} = \frac{|F_s|}{A} + \frac{|M_n|}{J}R \tag{1}$$

where the variables of A, I, and J = area, moment inertia, and polar moment inertia of the bonding disk, respectively, and are given by

$$A = \pi R^2, \qquad J = \frac{1}{2}\pi R^4, \qquad I = \frac{1}{4}\pi R^4 \tag{2}$$

If the maximum tensile stress exceeds the normal strength, or the maximum shear stress exceeds the shear strength, the parallel bond breaks. To dissipate the fracture energy generated in the breaking process of bonded particles, a softening bond model is implemented taking into account the elastic damage (Onate and Rojek 2004; Paavilainen et al. 2011; Tarokh and Fakhimi 2014). In this softening model, the normal stiffness at contact point is assumed to decrease linearly after the peak tensile force, and a softening stiffness K_{ns} is introduced into the force-displacement relationship, as shown in Fig. 2(a). Here, the softening stiffness is set as $K_{ns} = 0.5K_n$.

In this study, the normal tensile strength σ_n^b is set as a constant, while the shear strength is determined by the bonding strength in the shear direction and the friction induced by the normal stress following the Mohr-Coulomb friction law. The sliding friction coefficient between the two bonded particles, μ_b, is introduced here. Thus, the shear strength between two bonded particles considering the normal stress can be written as

$$\tau_b = \sigma_s^b + \mu_b \sigma_n \tag{3}$$

where τ_b = shear strength between bonded particles under the influence of normal stress; σ_s^b = interparticle shear bonding strength; μ_b = interparticle friction coefficient between the bonded particles; and σ_n = normal compressive stress of the bonded particles. Considering the contact area of the two bonded particles, the shear failure criterion is plotted as shown in Fig. 2(b). After the breakage of bonded particles, the interparticle cohesion is set to be zero, and the friction coefficient is set as μ for the separated particles.

In most previous investigations on failure criteria of bonded particles, the friction coefficient is $\mu_b = 0.0$. This means the interparticle shear strength is independent of the normal compressive stress. Recently, more researchers have paid attentions on the influence of normal compressive on the failure strength in tangential direction (Wang and Tonon 2010; Scholtes and Donze 2012; Nitka and Tejchman 2015). The ratio of cohesion to normal strength of bonded particles can be set a constant and written as

$$\alpha = \frac{\sigma_s^b}{\sigma_n^b} \tag{4}$$

The ratio α can be set as 1.0 or other values (Potyondy and Cundall 2004; Yang et al. 2006; Cho et al. 2007; Yang et al. 2014; Tarokh and Fakhimi 2014). In this study, the authors analyze its influence on the failure characteristics of brittle materials.

Considering the contact area of the bonded particles, the shear and normal stress can be switched to the force. Thus, Eq. (3) can be characterized as shown in Fig. 2(c). The maximum shear force

J. Eng. Mech., 2017, 143(1): C4016010

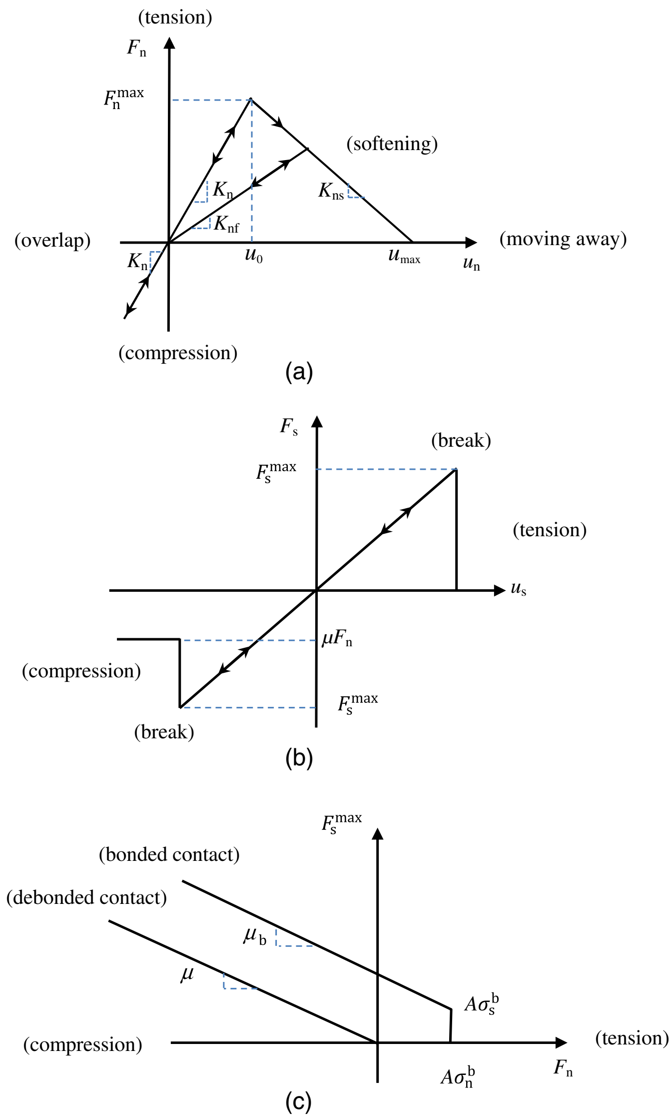

Fig. 2. Relationship in the softening contact bond model: (a) normal force and normal displacement; (b) shear force and shear displacement; (c) shear force and normal force

is determined by the normal force, cohesive force, and bonding friction coefficient (Hentz et al. 2004; Wang and Tonon 2010; Scholtes and Donze 2012; Nitka and Tejchman 2015).

In the tensile softening failure criterion, the normal stiffness changes with the damage degree between the two bonded particles during the progressive failure process (Tarokh and Fakhimi 2014). Here, the normal contact force in the damaged bond is given by

$$f = K_{nf} u_n = (1-\omega) K_n u_n \tag{5}$$

where K_{nf} = elastic damaged secant modulus; ω = scalar damage variable; and u_n = normal overlap between two contact particles. The scalar damage variable ω is a index of material damage. For the undamaged state, $\omega = 0$; for a damaged state, $0 < \omega \leq 1$. The scalar damage variable ω can be written as

$$\omega = \frac{\psi(u_n) - 1}{\psi(u_n)} \tag{6}$$

where $\psi(u_n)$ = function of the normal relative displacement. For a linear strain-softening criterion, $\psi(u_n)$ is defined by

$$\psi(u_n) = \begin{cases} 1 & \text{for } u_n \leq u_0 \\ \dfrac{K_n^2 u_n}{(K_{ns}+K_n)F_n^{\max} - K_{ns}K_n u_n} & \text{for } u_0 \leq u_n \leq u_{\max} \\ \infty & \text{for } u_n \geq u_{\max} \end{cases} \tag{7}$$

where $F_{\max}^n = A\sigma_n^b$; in which A = contact area of the two bonded particles; and $A = \pi R^2$.

A simple contact force-shear displacement law with damage can be introduced in the shear direction. The stiffness and the strength in shear direction decrease according to the damage state in the normal direction, and the reduction factor can be defined by

$$\lambda = \frac{\sigma_n^{b\prime}}{\sigma_n^b} \tag{8}$$

where $\sigma_n^{b\prime}$ = residual tensile strength of the bonded particles; and σ_n^b = initial cohesion of the bonded particles. When the contact bonds break due to damage, the Coulomb friction law is considered between the contact particles [Fig. 2(b)]. In this figure, $F_{\max}^s = A\lambda\sigma_s^b$.

The normal and shear stiffness between the two bonded particles can be defined with the mean radius of the bonding disk and the elastic modulus (Potyondy and Cundall 2004; Azevedo et al. 2015). The stiffness can be determined with (Wang and Tonon 2010; Nitka and Tejchman 2015)

$$K_n = E\frac{2R_A R_B}{R_A + R_B}, \qquad \beta = \frac{K_n}{K_s} \tag{9}$$

where the parameter β has a close realation with the Poisson's ratio (Tavarez and Plesha 2007; Weerasekara et al. 2013). In this study, $\beta = 2.0$.

DEM Simulations and Physical Experiments of Failure Processes of Sea Ice

DEM Simulations of Failure Processes of Sea Ice

Sea ice exhibits the mechanical properties of brittle material under rapid loading rate (Timco and Weeks 2010; Ji et al. 2011; Renshaw et al. 2014). In this study, the sea ice samples are constructed with the hexagonal close packing (HCP) pattern of spherical particles in three dimensions. In fact, the particles can be packed with different methods besides HCP, such as face-centered cubic (FCC) packing or random packing. For various packing patterns, the mechanical behaviors of sea ice are quite different in DEM simulations (Grof and Stepanek 2013; Liu et al. 2012). Moreover, the loading direction also has obvious influence on the failure process since the anisotropic behavior of sea ice samples. In field and laboratory tests of sea ice mechanical properties, the samples in uniaxial compressive tests and three-point bending tests are designed as $a \times a \times H = 100 \times 100 \times 250$ mm [as shown in Fig. 3(a)] and $b \times b \times L = 75 \times 75 \times 500$ mm [as shown in Fig. 4(a)], respectively (Ji et al. 2011). In the generations of the DEM samples with regular packing of spherical elements, the particle diameters are set as $D = 20$ and 16 mm for the uniaxial compression and three-point bending tests, respectively. The particle sizes are different in the two tests since the sea ice samples in DEM simulations are constructed to compare well with the physical tests. Here, the influence induced by the particle size difference can be ignored (Yang et al. 2006; Ding et al. 2014). The sea ice samples are constructed with the sizes of $a_1 \times a_2 \times H_1 = 100 \times 75 \times 228.6$ mm for the uniaxial

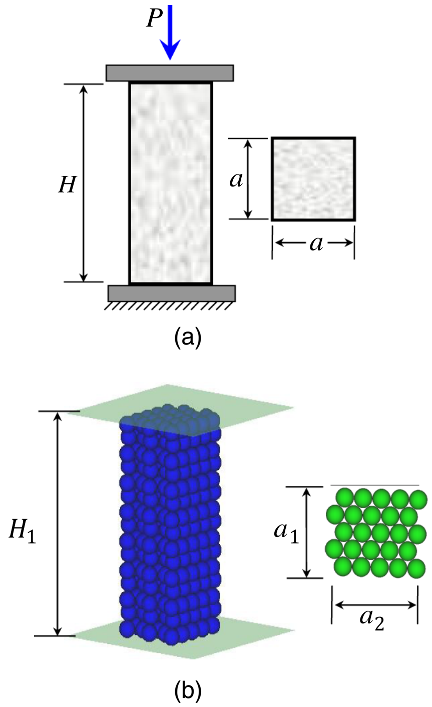

Fig. 3. Demonstration of the uniaxial compressive test of sea ice: (a) schematic diagram of sample; (b) numerical sample in DEM simulation

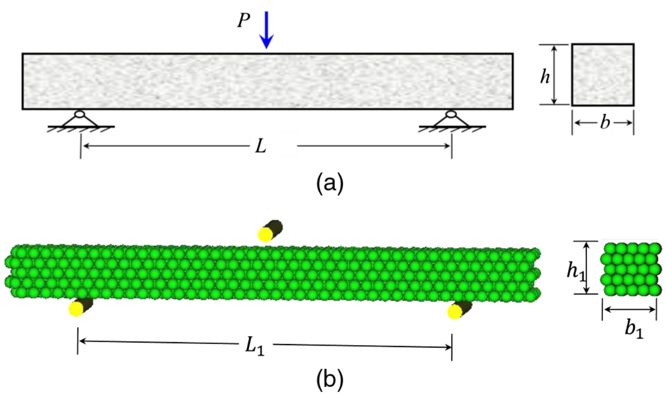

Fig. 4. Demonstration of the three-point bending test of sea ice: (a) schematic diagram of sample; (b) numerical sample in DEM simulation

compression test with 375 particles [as shown in Fig. 3(b)] and $b_1 \times b_2 \times L_1 = 52 \times 60 \times 500$ mm for the three-point bending test with 1,075 particles [as shown in Fig. 4(b)]. In the uniaxial compressive test, the bottom plate is fixed in the vertical direction and the top plate is given a constant downward loading speed. The friction coefficient between sea ice particles and loading plates are set as 0.1 here. In the three-point bending test, a constant downward vertical load is applied at the top center of the beam with a constant velocity. Two supporting columns and one loading column, which has contact with several particles, are applied on the surface of sea ice sample, as shown in Fig. 4(b). Some computational parameters are listed in Table 1.

For the uniaxial compression and three-point bending tests, the maximal loads are determined to calculate the uniaxial compressive and flexural strengths with

Table 1. Computational Parameters in the Discrete-Element Simulation of Sea Ice

Parameter	Symbol	Unit	Value
Elastic modulus	E	GPa	1.0
Ice density	ρ	kg/m^3	920
Interparticle tensile bonding strength	σ_n^b	MPa	0.74
Interparticle shear bonding strength	σ_s^b	MPa	$0.5\sigma_n^b$
Normal stiffness	K_n	N/m	$\pi DE/4$
Shear stiffness	K_s	N/m	$0.5K_n$
Softening normal stiffness	K_{ns}	N/m	$0.5K_n$
Friction coefficient between bonded particles	μ_b	—	0.0
Friction coefficient between separated particles	μ	—	0.1
Friction coefficient between particle and loading plates	μ_w	—	0.1
Particle diameter in uniaxial compression test	D	mm	16, 20

$$\sigma_c = \frac{P_{\max}}{a_1 a_2} \tag{10}$$

$$\sigma_f = \frac{3}{2}\frac{P_{\max} L_1}{b_1 h_1^2} \tag{11}$$

where $P_{\max}$ = maximum loading during the tests; the other parameters are shown in Figs. 3 and 4.

Figs. 5 and 6 show the failure process of the sea ice sample simulated with DEM under uniaxial compression and three-point bending. The results show the sea ice sample breaks in a shear failure pattern in compression test and breaks in a tensile fracture pattern in bending test. From the stress-strain curve of the compression test plotted in Fig. 7, the uniaxial compressive strength can be obtained with the maximum normal stress. For the three-point bending test, the flexural strength can be determined from the maximal normal stress, as shown in Fig. 8. For the two tests simulated with DEM described earlier, the uniaxial compressive strength $\sigma_c = 2.55$ MPa, and the flexural strength $\sigma_f = 1.59$ MPa.

Physical Experiments of Sea Ice Strength

To validate the preceding DEM results the physical experimental data of sea ice in the Bohai Sea are adopted here. The Bohai Sea locates in 37°0′N~41°0′N in latitude and 117°30′E~122°30′E in longitude. In the past several winters, the physical and mechanical properties of the sea ice have been measured in field and laboratory tests. Here, the uniaxial compressive strength and the flexural strength will be compared with the numerical results simulated with DEM. The macromechanical properties of sea ice, such as the uniaxial compressive strength and the flexural strength, are affected with the ice temperature, salinity, and loading rate (Timco and weeks 2010; Ji 2011). The brine volume (V_b) of sea ice can be written as a function of ice temperature and salinity, and is normally adopted to analyze the comprehensive influence of temperature and salinity (Timco and weeks 2010).

In the physical experiments of sea ice strengths, the samples are the same as these used in the DEM simulations. i.e., $a \times a \times H = 100 \times 100$ mm $\times$ 250 in uniaxial compressive tests and $b \times b \times L = 75 \times 75 \times 500$ mm in three-point bending tests. Under various brine volumes, the measured uniaxial compressive strength (σ_c) and flexural strength (σ_f) are plotted in Fig. 9. Here, the influence of loading rate is ignored since sea ice obviously performs the mechanical properties of brittle materials under rapid loading. In these physical experiments, 431 samples for uniaxial compression and 251 samples for three-point bending tests were carried out, respectively. From Fig. 9, it can be found that the measured sea ice strengths appear obvious randomness under the influence of ice

J. Eng. Mech., 2017, 143(1): C4016010

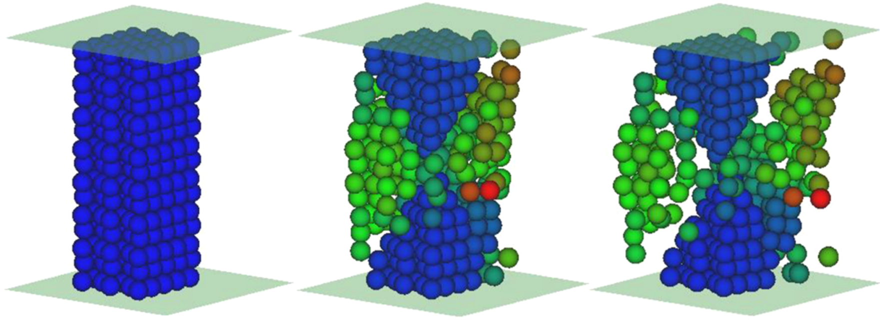

Fig. 5. Uniaxial compressive failure process of sea ice simulated with DEM; particle color represents the velocity of particles

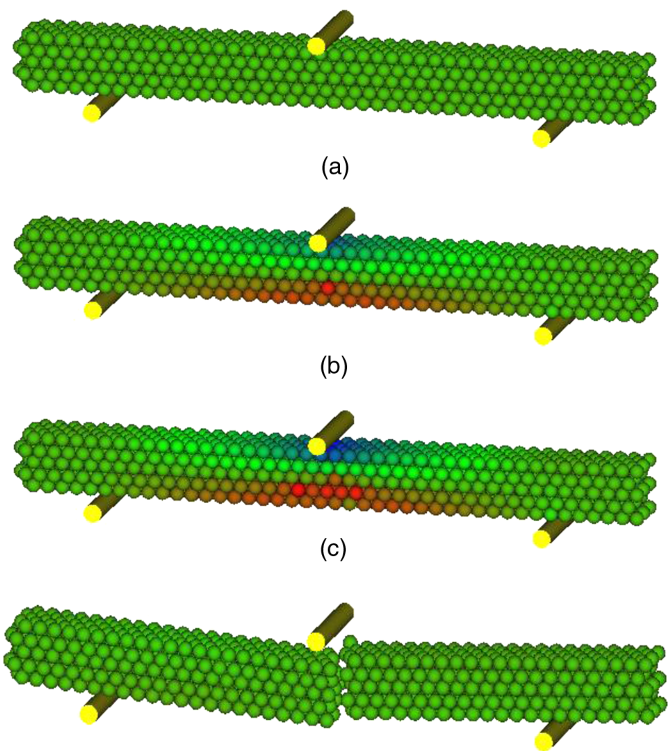

Fig. 6. Three-point bending failure process of sea ice simulated with DEM; particle color represents the normal interparticle contact force

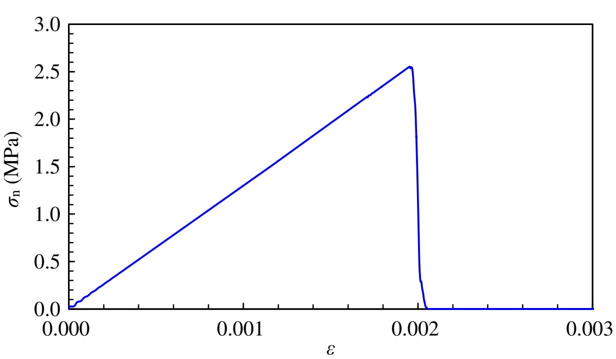

Fig. 7. Axial normal stress versus axial normal strain ice in compressive failure process of sea simulated with DEM

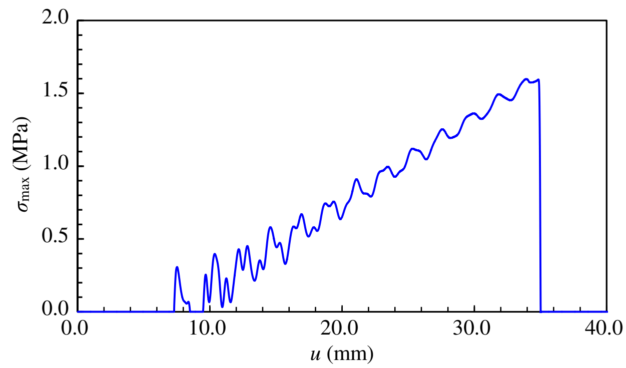

Fig. 8. Maximum normal stress versus vertical displacement in three-point bending failure process of sea ice simulated with DEM

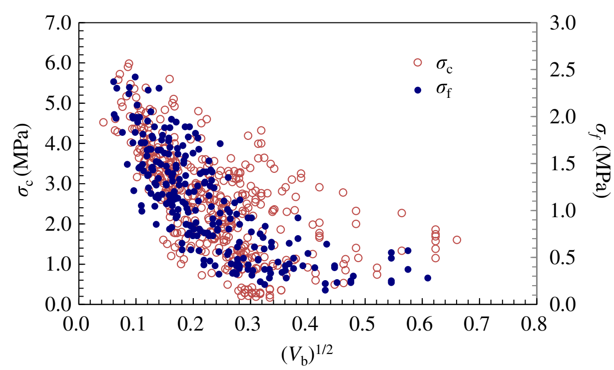

Fig. 9. Physical experimental results of uniaxial compressive strength and flexural strength of sea ice in the Bohai Sea

crystal structure. Since the size of ice crystal is much smaller than the particle size in DEM simulations, the influence of ice crystal on the macrostrength of sea ice cannot be considered well here. Thus, the statistical features of sea ice strengths are adopted to validate the DEM results. The maximum and mean values of σ_c are 5.98 MPa and 2.56 MPa, and the maximum and mean values of σ_f are 2.42 MPa and 1.08 MPa. Thus, the ratios of σ_c/σ_f are 2.47 and 2.37 for the maximum and mean values. From the numerical simulation of Figs. 7 and 8, the ratio $\sigma_c/\sigma_f = 1.60$. Besides the uniaxial compressive and flexural strengths, their ratio is also a very important parameter to validate the DEM simulation (Wang and Tonon 2010; Tarokn and Fakhimi 2014). In the following sections, the influence of interparticle strength and friction coefficient on the ratio of σ_c/σ_f will be investigated.

Relationship between Interparticle Bonding Strength and Macrostrength of Sea Ice in DEM Simulations

Influences of Interparticle Bonding Strengths on Failure Characteristics of Sea Ice

In the DEM simulations of sea ice compressive and flexural strengths presented earlier, the interparticle shear strength of bonded particles is set as constant without the consideration of the effect of normal pressure since the friction coefficient between bonded particles $\mu_b = 0.0$. The simulated strength ratio of sea ice $\sigma_c/\sigma_f = 1.60$, which is much smaller than that given in the physical data. The DEM simulations with bonded particles show the breaking pattern of sea ice sample exhibits shearing failure in uniaxial compression test (as shown in Fig. 5), and tensile failure in bending test (as shown in Fig. 6). Therefore, the simulated ratio of σ_c/σ_f can be increased with increasing the interparticle shear strength or decreasing the interparticle tensile strength. Here, the uniaxial compression and bending tests of sea ice samples are simulated with various interparticle tensile and shear strengths by σ_n^b and $\sigma_s^b = 0.1$, 0.25, 0.5, 0.75, 1.0, 1.5, and 2.0 MPa, respectively. The sample sizes are same as the DEM simulation given earlier, and the computational parameters used are listed in Table 1. With various interparticle tensile and shear strengths, the simulated contours of macrocompressive and flexural strengths are plotted in Figs. 10(a and b), and the contours of the macrostrength ratio of σ_c/σ_f are plotted in Fig. 10(c).

Figs. 10(a and b) show that both of the compressive and flexural strengths increase with increasing interparticle shear and tensile bonding strengths simultaneously. Increasing shear or tensile strength only, the simulated macrostrength has different dependency on the other interparticle strength. Two aided straight lines added from the origin of coordinates in each figure. In the region below the bottom line or above the top line, the contours approach horizontal or vertical trends. This indicates that the macrostrengths simulated with DEM are independent of the interparticle shear or tensile strength. Increasing the interparticle shear and tensile strengths together, the macrostrengths obviously increase. In the region below the bottom line, macrostrength is independent of the interparticle tensile strength, and is dominated by microshear strength. Under this situation, interparticle bonding is broken via shear failure criteria since the weakness of microshear strength.

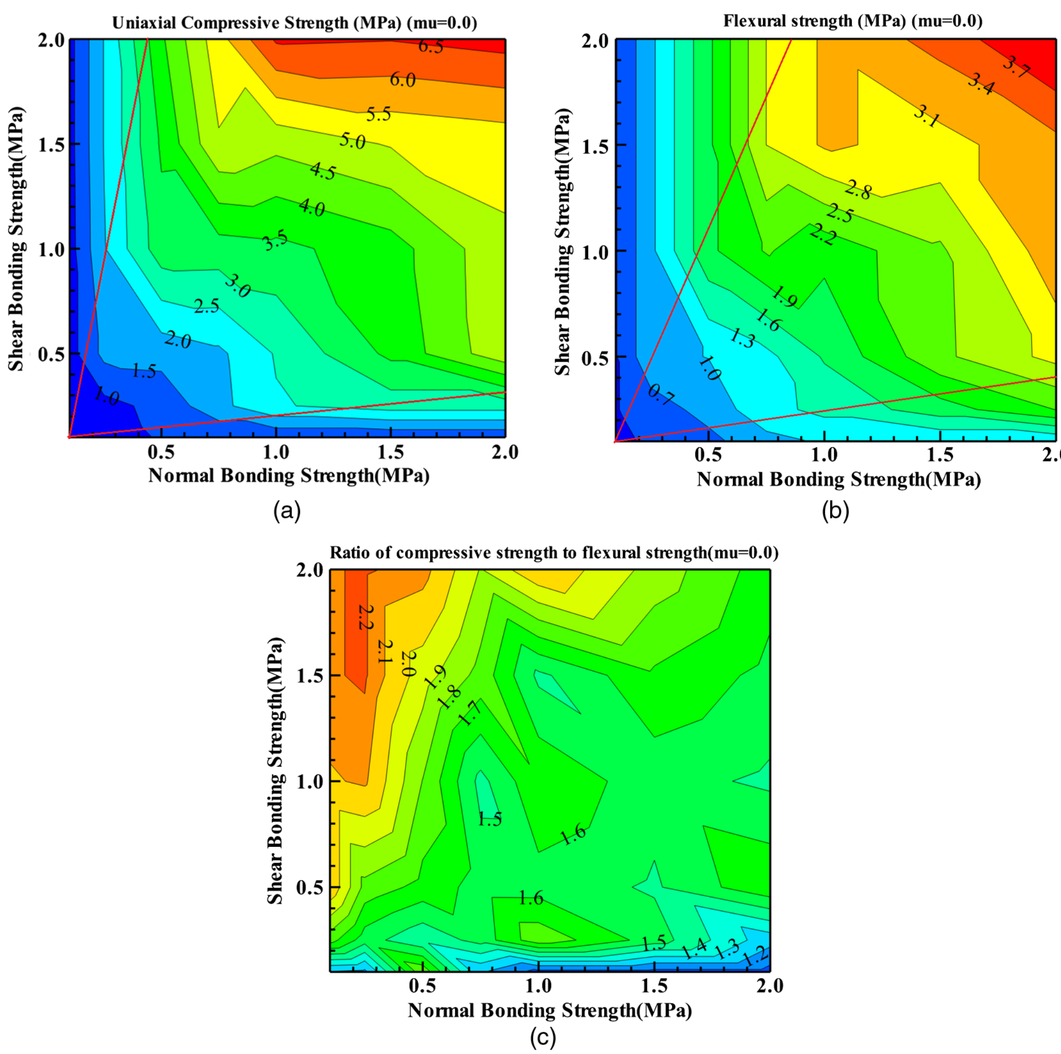

Fig. 10. Contour of the simulated macrostrengths of sea ice and strength ratio when $\mu_b = 0.0$: (a) uniaxial compressive strength; (b) flexural strength; (c) ratio of uniaxial compressive to flexural strength

In the other hand, in the region above the top line, macrostrength is dominated by microtensile strength. Interparticle bonding is broken normally via tensile failure criteria given the weakness of microtensile strength.

From the contour of the macrostrength ratio of σ_c/σ_f [as shown in Fig. 10(c)], the ratio increases from 1.2 to 2.1 with increasing interparticle shear strength. But the maximum ratio simulated here is still smaller than that obtained in physical experiments, as shown in Fig. 9. In the earlier DEM simulations, the interparticle friction coefficient between bonded particles is ignored. When considering the influence of interparticle friction on the shear criterion, as shown in Fig. 2(c), the interparticle shear strength will be increased.

Influences of Interparticle Friction of Bonded Particles on Failure Characteristics of Sea Ice

The interparticle friction coefficient of bonded particles μ_b has significant influence on the macromechanical properties in DEM simulations (Wang and Tonon 2010; Estay and Chiang 2013; Nitka and Tejchman 2015). Here, the value of μ_b is set as 0.1, 0.2, and 0.3 to simulate the uniaxial compressive and three-point bending tests. The simulated contours of compression strength (σ_c), flexural strength (σ_f), and ratio of σ_c/σ_f are plotted in Figs. 11–13. Similar to the results simulated with $\mu_b = 0.0$, the macroscale uniaxial compressive and flexural strengths increase with increasing interparticle shear and tensile strength. In each figure, two aided straight lines are added from the origin of coordinates to show the contour distributions. In the region below the bottom line or above the top line, the contours are parallel to the horizontal or vertical coordinate. This means macrostrength is not sensitive to microbonding strength in those domains.

Comparing the uniaxial compressive strength σ_c simulated with various interparticle friction μ_b [as shown in Figs. 10(a), 11(a), 12(a) and 13(a)], it can be found that σ_c increases with the increase of μ_b. The angle between the two aided straight lines decreases with increasing μ_b, and close to the line of $\sigma_n^b = \sigma_s^b$. This indicates that the interparticle friction plays a more significant effect on the compressive strength. But from the contours plotted in Figs. 10(b), 11(b), 12(b) and 13(b), the flexural strength is independent of the interparticle friction since the interparticle bonding disks are broken via tensile failure in the bending tests.

From the contours of σ_c/σ_f simulated with $\mu_b = 0.1$ in Figs. 11(c), it can be found that the ratio of σ_c/σ_f increases with increasing shear bonding strength or decreasing tensile strength. This trend is similar as that simulated with $\mu_b = 0.0$ in Fig. 10(c). However, from the contours simulated with $\mu_b = 0.2$ and 0.3 in Figs. 12(c) and 13(c), the ratio has a high value in the zone close to $\sigma_n^b = \sigma_s^b$. The ratio of σ_c/σ_f is close to 2.6 and 3.5 when $\mu_b =$ 0.2 and 0.3, respectively. The mean ratio is 2.37 in the physical experiments of sea ice in the Bohai Sea. Therefore, the reasonable parameter for the DEM simulation of sea ice failure process can be obtained as $\mu_b = 0.2$, and $\sigma_n^b = \sigma_s^b$. Based on the simulated data when $\sigma_n^b = \sigma_s^b$, the relationship between interparticle friction

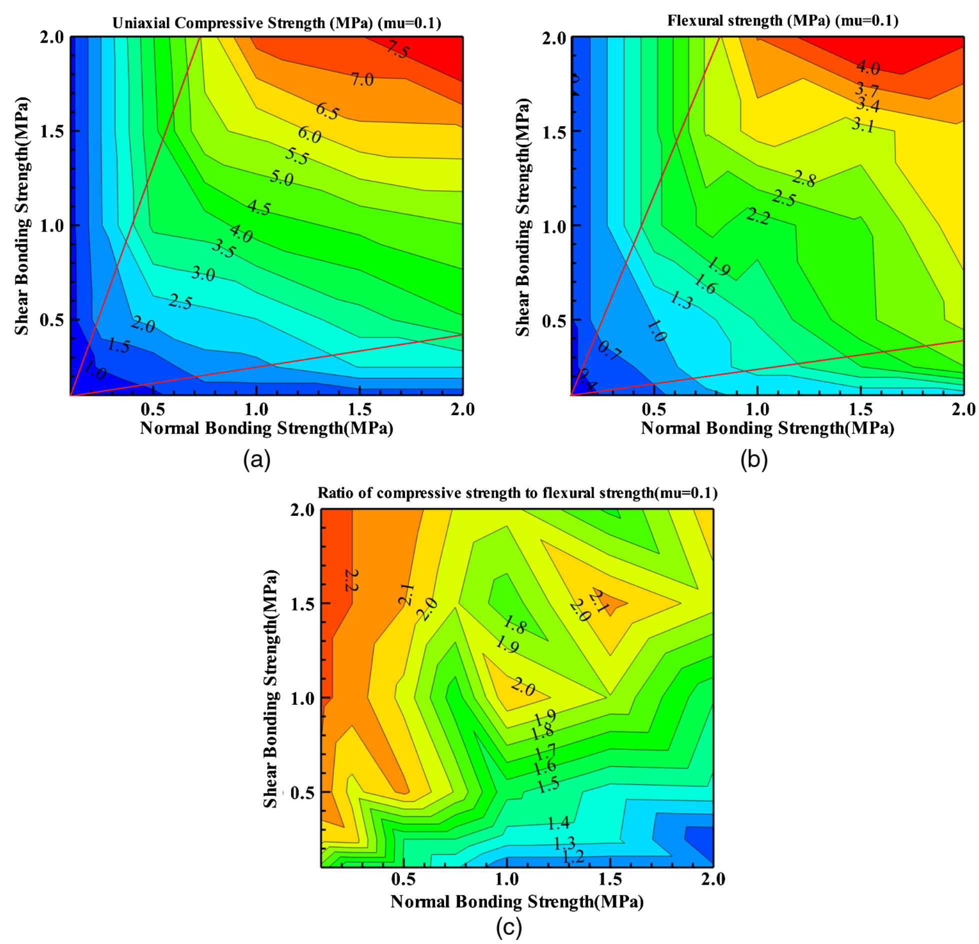

Fig. 11. Contour of the simulated macrostrengths of sea ice and strength ratio when $\mu_b = 0.1$: (a) uniaxial compressive strength; (b) flexural strength; (c) ratio of uniaxial compressive to flexural strength

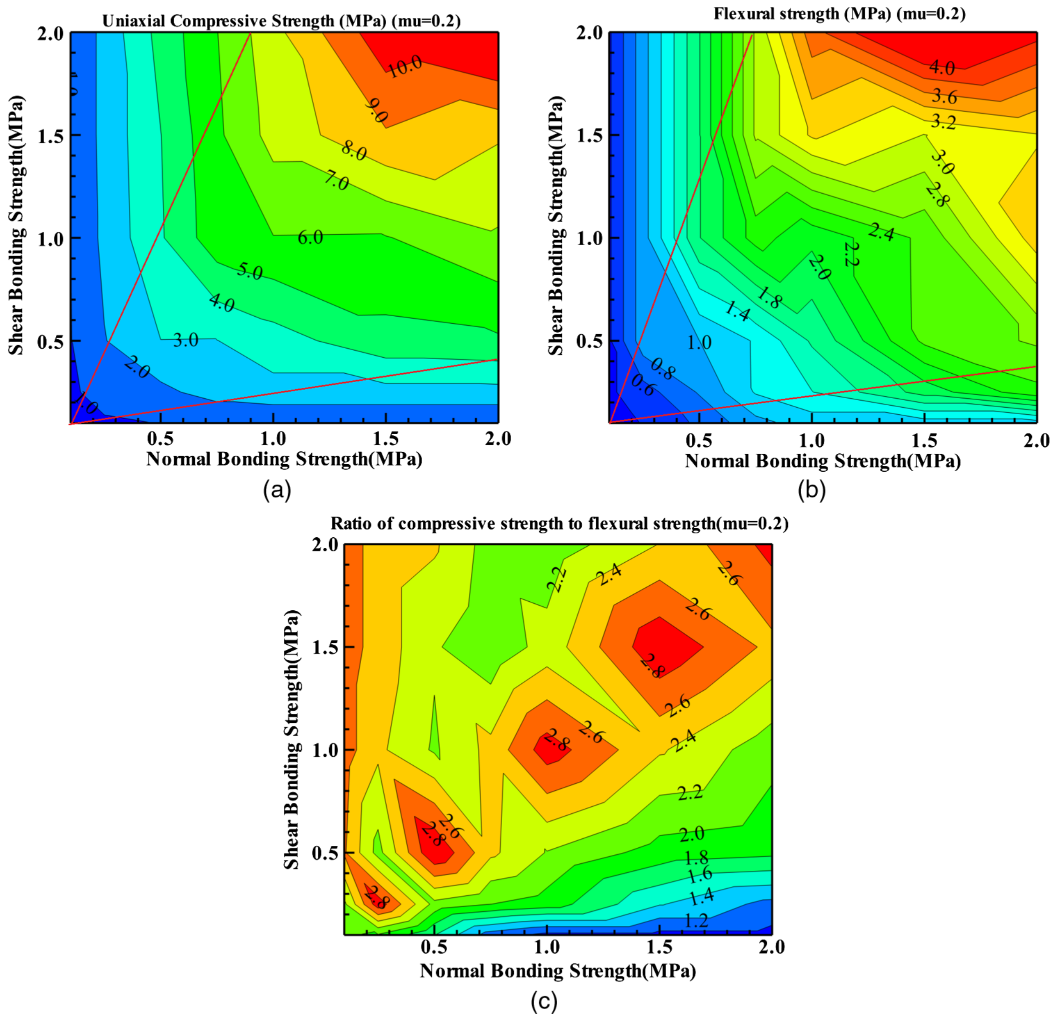

Fig. 12. Contour of the simulated macrostrengths of sea ice and strength ratio when $\mu_b = 0.2$: (a) uniaxial compressive strength; (b) flexural strength; (c) ratio of uniaxial compressive to flexural strength

coefficient and strength ratio of σ_c/σ_f can be obtained as shown in Fig. 14, and can be written as

$$\frac{\sigma_c}{\sigma_f} = 6.59\mu_b + 1.57 \tag{12}$$

With Eq. (12), the interparticle friction coefficient can be determined for a given ratio of σ_c/σ_f. The macrostrength of sea ice is affected by the ice brine volume, which is a function of temperature and salinity, ice crystals, and loading rate. Therefore, the interparticle strength on the microscale can be defined according to the macrostrength of sea ice material considering the factors given earlier.

Relationship between Interparticle Strength and Macrostrength of Sea Ice

When the interparticle tensile and shear strengths are set as the same value, i.e., $\sigma_b = \sigma_n^b = \sigma_s^b$, the relation between microparameters and macrostrengths of sea ice can be determined with the DEM results. Under various interparticle friction coefficients (μ_b), the simulated uniaxial compressive strength is plotted in Fig. 15(a). It shows the uniaxial compressive strength (σ_c) increases linearly with interparticle bonding strength (σ_b) when μ_b is constant. For each line of a given μ_b, the slope is the ratio of σ_c/σ_b. Here, this ratio is plotted versus μ_b in Fig. 15(b). The relationship between interparticle friction of bonded particles, interparticle strength, and uniaxial compressive strength is

$$\frac{\sigma_c}{\sigma_b} = 13.27\mu_b + 3.19 \tag{13}$$

where σ_b = interparticle tensile and shear strength.

The simulated flexural strength (σ_f) under various microstrengths and interparticle friction coefficients are plotted in Fig. 16(a). It shows the value of σ_f is independent of μ_b, and increases linearly with the increase of σ_b. The relationship between σ_f and σ_b is plotted in Fig. 16(b) and can be written as

$$\sigma_f = 2.03\sigma_b \tag{14}$$

From Eqs. (13) and (14), it can be found that μ_b only affects the uniaxial compressive strength (σ_c), and the flexural strength (σ_f) is not sensitive on μ_b. In uniaxial compression tests, the sea ice sample fractures in a shear pattern accompanying the shear failure of interparticle bonding. The interparticle shear strength τ_b is dominated by both of μ_b and σ_b, as shown in Eq. (3). In bending tests, the bonding disks mainly break in a tensile pattern, and tensile strength is independent of μ_b.

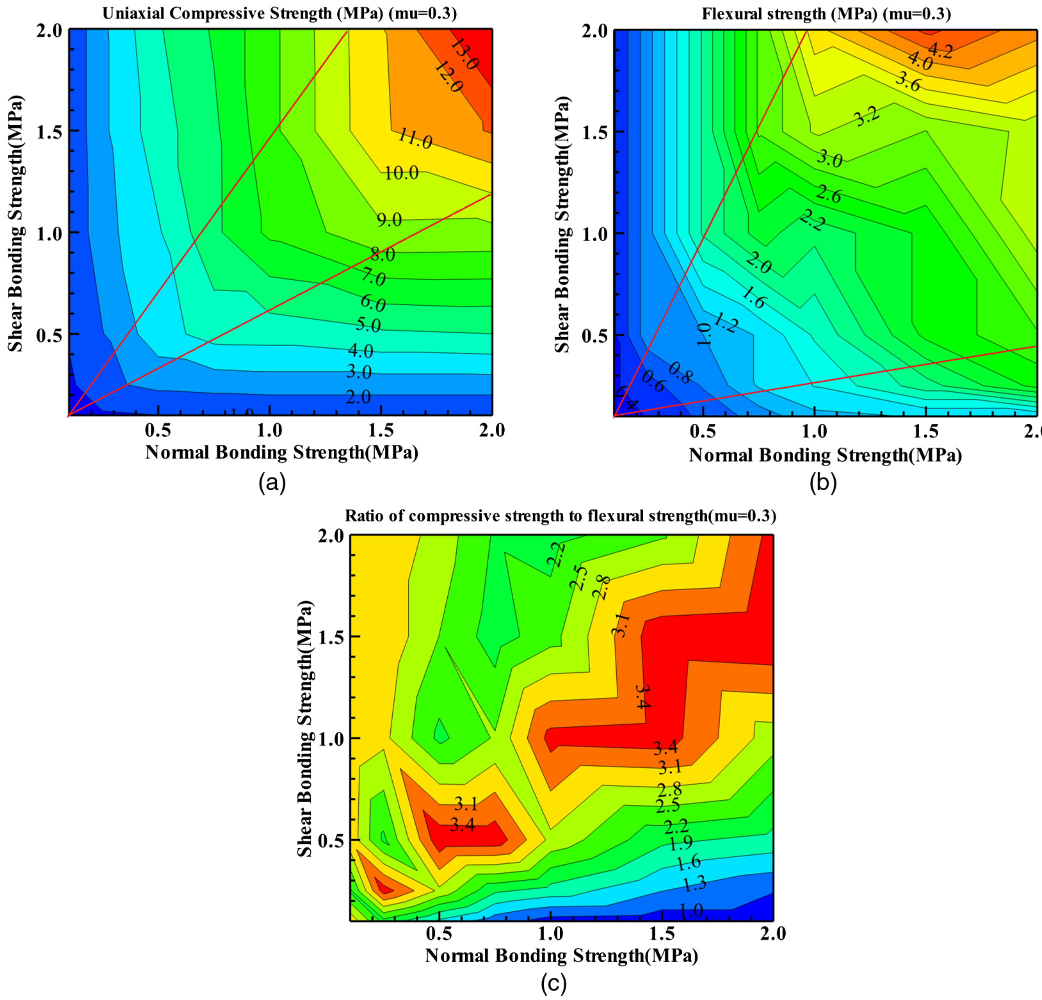

Fig. 13. Contour of the simulated macrostrengths of sea ice and strength ratio when $\mu_b = 0.3$: (a) uniaxial compressive strength; (b) flexural strength; (c) ratio of uniaxial compressive to flexural strength

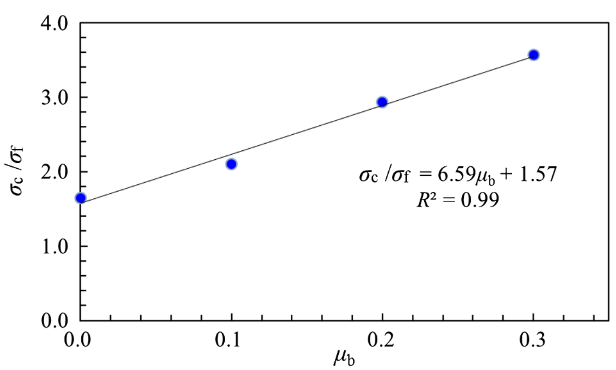

Fig. 14. Relationship between interparticle friction coefficient μ_b and strength ratio of σ_c/σ_f

Conclusions

A three-dimensional discrete-element method (DEM) with bonded particles is adopted to simulate the failure process of brittle materials. The tension softening failure criterion considering the influence of interparticle friction of bonded particles is developed to model the uniaxial compression and three-point bending tests of sea ice samples. The simulated macrostrength, especially the ratio of uniaxial compressive to flexural strength, is compared with the physical experimental data of the Bohai sea ice. The influences of microbonding strength and interparticle friction coefficient on the macrostrength of sea ice are discussed based on the DEM results. The simulated macrostrength increases with increasing both the interparticle shear and tensile strengths. The increase of the interparticle friction coefficient of bonded particles increase the macroscale uniaxial compressive strength, and does not affect the flexural strength of sea ice. When the microscale tensile and shear strengths are set the same, and the interparticle friction is set as 0.2, the reasonable macrostrengths of sea ice can be simulated with DEM. The relationship between the macrostrength of continuum material and the microstrength of bonded particles are determined.

In this study, the influence of interparticle bonding strengths are analyzed in terms of the failure processes of sea ice with DEM simulations. All of the other parameters are fixed in the DEM simulations, such as the ratio of shear to normal stiffness, ratio of sample to particle size, interparticle friction of unbonded particles, and packing pattern of particles. The parameters used in this paper can be adopted to simulate the brittle failure process of sea ice. Even so, the influences of temperature and salinity, ice crystals, and loading rate are not considered in the present work. In the close future study, the interbonding strength will be defined as a function of loading rate, temperature, and salinity. The anisotropic properties

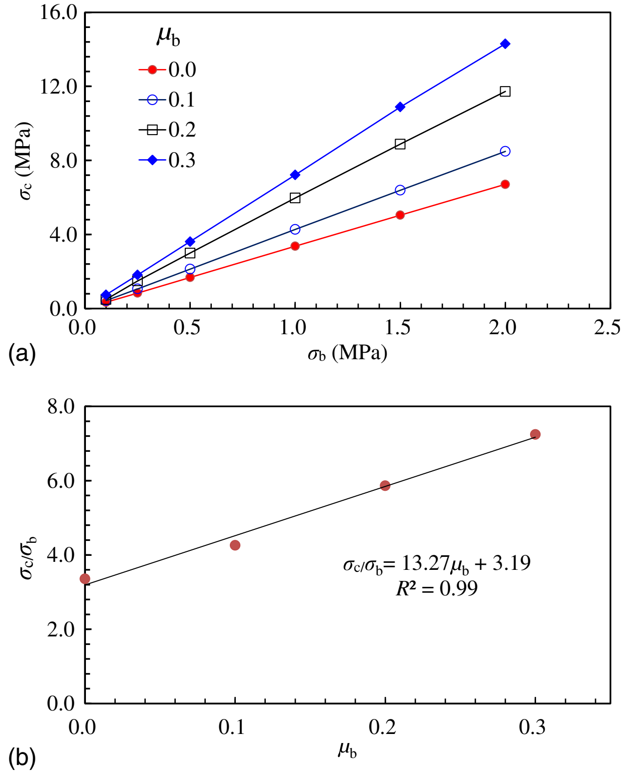

Fig. 15. Influence of interparticle bonding strength and friction coefficient of bonded particles on the uniaxial compressive strength and of sea ice: (a) uniaxial compressive strength versus interparticle bonding strength; (b) uniaxial compressive strength versus interparticle friction coefficient

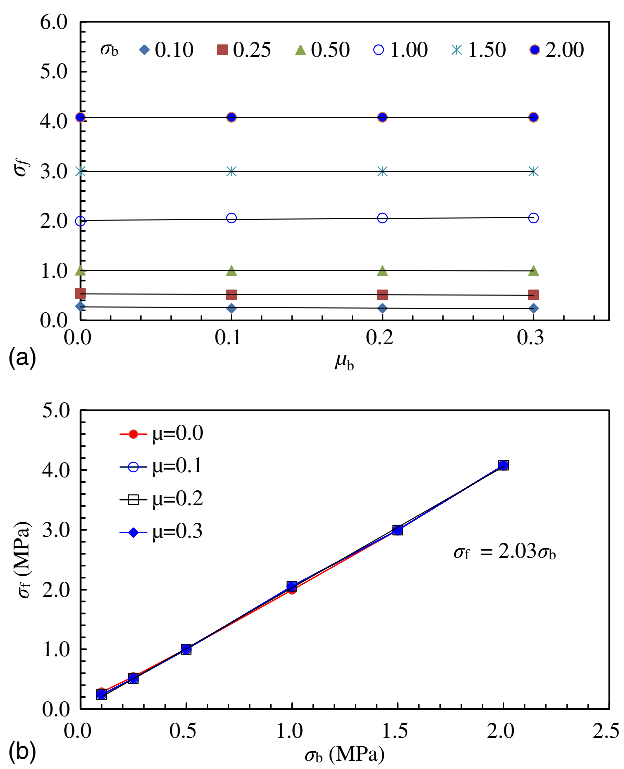

Fig. 16. Influence of interparticle bonding strength and friction coefficient of bonded particles on the flexural strength and of sea ice: (a) macroflexural strength versus interparticle friction coefficient; (b) macroflexural strength versus interparticle strength

of sea ice under the influence of a crystal structure will be also considered. But for other materials, such as rock, the influence of microparameters on particle scale will be investigated comprehensively to obtain rational parameters in DEM simulations.

Acknowledgments

This study is financially supported by the Special Funding for National Marine Commonwealth Industry of China (Grant Nos. 201105016, 201205007), the National Natural Science Foundation of China (Grant Nos. 41176012, 11372067), and the Fundamental Research Funds for the Central Universities (DUT15ZD105).

References

Ali, A. Y., and Bradshaw, S. M. (2010). "Bonded-particle modelling of microwave-induced damage in ore particles." *Miner. Eng.*, 23(10), 780–790.

Azevedo, N., Candeias, M., and Gouveia, F. (2015). "A rigid particle model for rock fracture following the Voronoi tessellation of the grain structure: Formulation and validation." *Rock Mech. Rock Eng.*, 48(2), 535–557.

Brown, N. J., Chen, J. F., and Ooi, J. Y. (2014). "A bond model for DEM simulation of cementitious materials and deformable structures." *Granular Matter*, 16(3), 299–311.

Cho, N., Martin, C. D., and Sego, D. C. (2007). "A clumped particle model for rock." *Int. J. Rock Mech. Min. Sci.*, 44(7), 997–1010.

Ding, X., Zhang, L., Zhu, H., and Zhang, Q. (2014). "Effect of model scale and particle size distribution on PFC3D simulation results." *Rock Mech. Rock Eng.*, 47(6), 2139–2156.

Ergenzinger, C., Seifried, R., and Eberhard, P. (2012). "A discrete element model predicting the strength of ballast stones." *Comput. Struct.*, 108/109, 3–13.

Estay, D. A., and Chiang, L. E. (2013). "Discrete crack model for simulating rock comminution processes with the discrete element method." *Int. J. Rock Mech. Min. Sci.*, 60, 125–133.

Feng, Y. T., and Owen, D. R. J. (2014). "Discrete element modelling of large scale particle systems-I: Exact scaling laws." *Comput. Particle Mech.*, 1(2), 159–168.

Grof, Z., and Stepanek, F. (2013). "Distribution of breakage events in random packings of rodlike particles." *Phys. Rev. E*, 88(1), 012205.

Hanley, K. J., O'sullivan, C., Oliveira, J. C., Cronin, K., and Byrne, E. P. (2011). "Application of Taguchi methods to DEM calibration of bonded agglomerates." *Powder Technol.*, 210(3), 230–240.

Hashemi, S. S., Momeni, A. A., and Melkoumian, N. (2014). "Investigation of borehole stability in poorly cemented granular formations by discrete element method." *J. Pet. Sci. Eng.*, 113, 23–35.

Hentz, S. D., Daudeville, L., and Donze, F. V. (2004). "Identification and validation of a discrete element model for concrete." *J. Eng. Mech.*, 10.1061/(ASCE)0733-9399(2004)130:6(709), 709–719.

Hosseininia, E. S., and Mirghasemi, A. A. (2007). "Effect of particle breakage on the behavior of simulated angular particle assemblies." *China Particuology*, 5(5), 328–336.

Huang, J., Xu, S., and Hu, S. (2014). "Influence of particle breakage on the dynamic compression responses of brittle granular materials." *Mech. Mater.*, 68, 15–28.

Ji, S., Wang, A., Jie, S., and Yue, Q., (2011). "Experimental studies on elastic modulus and flexural strength of sea ice in the Bohai Sea." *J. Cold Reg. Eng.*, 10.1061/(ASCE)CR.1943-5495.0000035, 182–195.

Kuhn, M. R., and Bagi, K. (2009). "Specimen size effect in discrete element simulations of granular assemblies." *J. Eng. Mech.*, 10.1061/(ASCE)0733-9399(2009)135:6(485), 485–492.

Lisjak, A., and Grasselli, G. (2014). "A review of discrete modeling techniques for fracturing processes in discontinuous rock masses." *J. Rock Mech. Geotech. Eng.*, 6(4), 301–314.

Liu, C., Pollard, D. D., and Shi, B. (2013). "Analytical solutions and numerical tests of elastic and failure behaviors of close-packed lattice for brittle rocks and crystals." *J. Geophys. Res. Solid Earth*, 118(1), 71–82.

Liu, Y., You, Z., and Zhao, Y., (2012). "Three-dimensional discrete element modeling of asphalt concrete: Size effects of elements." *Constr. Build. Mater.*, 37, 775–782.

Metzger, M. J., and Glasser, B. J. (2012). "Numerical investigation of the breakage of bonded agglomerates during impact." *Powder Technol.*, 217, 304–314.

Nitka, M., and Tejchman, J., (2015). "Modelling of concrete behaviour in uniaxial compression and tension with DEM." *Granular Matter*, 17(1), 145–164.

Onate, E., and Rojek, J. (2004). "Combination of discrete element and finite element methods for dynamic analysis of geomechanics problems." *Comput. Methods Appl. Mech. Eng.*, 193, 3087–3128.

Paavilainen, J., Tuhkuri, J., and Polojarvi, A. (2011). "2D numerical simulations of ice rubble formation process against an inclined structure." *Cold Reg. Sci. Technol.*, 68(1–2), 20–34.

Park, J. W., and Song, J. J. (2009). "Numerical simulation of a direct shear test on a rock joint using a bonded-particle model." *Int. J. Rock Mech. Min. Sci.*, 46(8), 1315–1328.

Park, J. W., and Song, J. J. (2013). "Numerical method for the determination of contact areas of a rock joint under normal and shear loads." *Int. J. Rock Mech. Min. Sci.*, 58, 8–22.

Potyondy, D. O., and Cundall, P. A. (2004). "A bonded-particle model for rock." *Int. J. Rock Mech. Min. Sci.*, 41(8), 1329–1364.

Renshaw, C. E., Golding, N., and Schulson, E. M. (2014). "Maps for brittle and brittle-like failure in ice." *Cold Reg. Sci. Technol.*, 97, 1–6.

Rojek, J., Onate, E., Labra, C., and Kargl, H., (2011). "Discrete element simulation of rock cutting." *Int. J. Rock Mech. Min. Sci.*, 48(6), 996–1010.

Scholtes, L., and Donze, F.-V. (2012). "Modelling progressive failure in fractured rock masses using a 3D discrete element method." *Int. J. Rock Mech. Min. Sci.*, 52, 18–30.

Tarokh, A., and Fakhimi, A. (2014). "Discrete element simulation of the effect of particle size on the size of fracture process zone in quasi-brittle materials." *Comput. Geotech.*, 62, 51–60.

Tavarez, F. A., and Plesha, M. E. (2007). "Discrete element method for modelling solid and particulate materials." *Int. J. Numer. Methods Eng.*, 70(4), 379–404.

Timco, G. W., and Weeks, W. F. (2010). "A review of the engineering properties of sea ice." *Cold Reg. Sci. Technol.*, 60(2), 107–129.

van Wyk, G., Els, D. N. J., Akdogan, G., Bradshaw, S. M., and Sacks, N. (2014). "Discrete element simulation of tribological interactions in rock cutting." *Int. J. Rock Mech. Min. Sci.*, 65, 8–19.

Wang, Y. (2009). "A new algorithm to model the dynamics of 3-D bonded rigid bodies with rotations." *Acta Geotech.*, 4(2), 117–127.

Wang, Y., and Tonon, F. (2009). "Modeling Lac du Bonnet granite using a discrete element model." *Int. J. Rock Mech Min. Sci.*, 46(7), 1124–1135.

Wang, Y., and Tonon, F. (2010). "Calibration of a discrete element model for intact rock up to its peak strength." *Int. J. Numer. Anal. Methods Geomech.*, 34(5), 447–469.

Weerasekara, N. S., et al. (2013). "The contribution of DEM to the science of comminution." *Powder Technol.*, 248, 3–24.

Yan, Y., Zhao, J., and Ji, S. (2015). "Discrete element analysis of breakage of irregularly shaped railway ballast." *Geomech. Geoeng. Int. J.*, 10(1), 1–9.

Yang, B., Jiao, Y., and Lei, S. (2006). "A study on the effects of microparameters on macroproperties for specimens created by bonded particles." *Eng. Comput.*, 23(6), 607–631.

Yang, S. Q., Huang, Y. H., Jing, H. W., and Liu, X. R. (2014). "Discrete element modeling on fracture coalescence behavior of red sandstone containing two unparallel fissures under uniaxial compression." *Eng. Geol.*, 178, 28–48.

J. Eng. Mech., 2017, 143(1): C4016010